*Aerosol and Air Quality Research*, 19: 1421–1438, 2019

ISSN: 1680-8584 print / 2071-1409 online
doi: 10.4209/aaqr.2018.10.0389

# Preparation of Cu-Mn and Cu-Mn-Ce Oxide-incorporated Mesoporous Silica via Silicate Exfoliation for the Removal of NO and $Hg^0$

**Cong-Jhen Lin[1], Chuan-Lin Chang[2], Chih-Fu Tseng[1,3], Hong-Ping Lin[2*], Hsing-Cheng Hsi[1*]**

[1] *Graduate Institute of Environmental Engineering, National Taiwan University, Taipei 10617, Taiwan*
[2] *Department of Chemistry, National Cheng-Kung University, Tainan 70101, Taiwan*
[3] *Taiwan Power Research Institute, Taiwan Power Company, New Taipei City 23847, Taiwan*

## ABSTRACT

Cu-Mn and Cu-Mn-Ce oxide-incorporated mesoporous silica was formed by hydrothermally exfoliating silicate, and the physicochemical properties and NO/$Hg^0$ removal efficiency were investigated. The exfoliation induced structural reformation, resulting in a large specific surface area and the uniform dispersion of metal oxides on the surface. The transfer of valences between $Cu^{2+}$ and $Mn^{3+}$ in the Cu-Mn silica contributed to the single reduction peak displayed in the $H_2$ temperature-programmed reduction profiles and the high $Mn^{4+}$/Mn and $Cu^{+}$/Cu ratios observed via X-ray photoelectron spectroscopy (XPS). The high oxygen lability of the Cu-Mn silica may have inhibited its ability to remove NO. By contrast, when $SO_2$ was present, incorporating Ce enhanced the NO removal efficiency due to the increased number of Brønsted acid sites. $Hg^0$ removal tests indicated that adsorption was the primary removal mechanism for both the Cu-Mn and the Cu-Mn-Ce silica samples. Cu2Mn8 exhibited the highest Hg removal efficiency, suggesting that Ce's enhancing effect on $Hg^0$ adsorption was diminished when a large amount of Mn was present. Of the gaseous components, the adsorbed HCl was mainly responsible for the oxidation and subsequent adsorption of $Hg^0$. Furthermore, with the addition of $SO_2$, the competitive adsorption of $SO_2$ and the resulting $HgCl_2$ did not decrease the Cu-Mn silica's efficiency in oxidizing $Hg^0$, but the oxidized Hg was less adsorptive.

***Keywords:*** Silicate exfoliation; Coal combustion; Mercury; Multi-pollutant; Metal oxide.

## INTRODUCTION

Coal-fired power plants (CFPPs) have been reported as one of the major anthropogenic emission sources of $NO_x$, $SO_2$, and heavy metals, such as mercury (U.S. EPA, 2012; UNEP, 2013). $NO_x$ plays a major role in the photochemical reactions in the troposphere and stratosphere, which further cause severe environmental impacts, namely, acid rain and photochemical smog (Roy *et al.*, 2009). Mercury has received great concerns on its influences on both human health and the living environment due to its high toxicity, persistence, and long-distance transport (Chen *et al.*, 2016; Marusczak *et al.*, 2016; Guo *et al.*, 2017). In CFPPs, mercury mainly exists in three forms in the gas streams: elemental mercury ($Hg^0$), oxidized mercury ($Hg^{2+}$), and particle-bound mercury ($Hg^p$) (Galbreath and Zygarlicke, 2000). Most of $Hg^{2+}$ and $Hg^p$ could be adequately removed by the conventional air pollution control devices. $Hg^{2+}$ can be removed by wet flue gas desulfurization and $Hg^p$ is primarily removed by electrostatic precipitator and fiber filter. However, $Hg^0$ is difficult to be removed due to its high stability and volatility (Zhao *et al*., 2019).

Instead of using the high-cost activated carbon injection for direct adsorption to transform $Hg^0$ into $Hg^p$ (Chou *et al.*, 2018), catalytic oxidation of $Hg^0$ to $Hg^{2+}$ and subsequently to $Hg^p$ over selective catalytic reduction (SCR) catalysts could be a co-benefit during traditional NO removal by metal oxide catalysts. $Hg^0$ catalytic oxidation by various metal oxide catalysts in simulated flue gas has also been examined (Wang *et al.*, 2014; Xiong *et al.*, 2017). Some research has also been done on understanding the simultaneous removal of $Hg^0$ and NO (He *et al.*, 2013; Chang *et al.*, 2015; Li *et al.*, 2015; Zhao *et al.*, 2016; Song *et al.*, 2018). The removal effectiveness of $Hg^0$ by the catalysts depends on the operating environment (flue gas composition and temperature) and the properties of the catalysts (Li *et al.*, 2011a). The addition of ammonia for reduction of $NO_x$ may inhibit the $Hg^0$ removal due to competition of adsorption sites on the catalyst surface (Chang *et al.*, 2015).

Mn-Ce oxides have been widely studied as low-

* Corresponding authors.
Tel.: +886 2 33664374; Fax: +886 2 23928830
*E-mail address:* hchsi@ntu.edu.tw (H.C. Hsi);
hplin@mail.ncku.edu.tw (H.P. Lin)

temperature SCR catalysts due to the presence of various valence states for Mn/Ce and their labile oxygen (Wang *et al.*, 2014). Kang *et al.* (2006) showed that the $NO_x$ conversion of $MnO_x$ could keep over 95% at temperature below 175°C; in the same study, Cu-Mn mixed oxides showed over 95% NO removal efficiency at a broader temperature window (50–250°C). Fang *et al.* (2014) addressed that $CuMn_2O_4$ spinel in Cu-Mn mixed oxide catalysts could promote the valence transition between $Cu^{2+}$ and $Mn^{3+}$ that promoted the SCR performance. The mixture of metallic species can enhance the effects towards an increment in the mobility of the oxygen, as well as stabilizing the active species and favoring the redox cycles that permits the reactivation of the catalyst (Aguilera *et al.*, 2011). Ce oxide has also been known to have a great oxygen storage capacity and outstanding redox characteristics and can be a promising additive for low-temperature $NH_3$-SCR (Xu *et al.*, 2018). Our earlier studies have also shown that activated carbon and zeolite impregnated with Cu oxide and Cu chloride had great $Hg^0$ adsorption performance (Chiu *et al.*, 2014, 2015; Tsai *et al.*, 2017). Therefore, a combination of Cu-Mn or Cu-Mn-Ce oxides supported by porous materials, such as $SiO_2$, could possess great effectiveness in NO reduction and $Hg^0$ oxidation followed by subsequent adsorption. A summary of selected studies on Cu and Mn oxide catalysts for NO and $Hg^0$ removal is shown in Table 1.

The difference in crystallinity, oxidation state, and the amount of specific surface area and pore volume of metal oxides supported by porous materials could influence the NO and $Hg^0$ removal performance. Therefore, a novel silicate exfoliation method was applied in this study to synthesize the Cu-Mn and Cu-Mn-Ce mixed oxides supported by mesoporous silica. During the silicate exfoliation method, the proper hydrothermal treatment could cause the surface structure of $SiO_2$ to reform. The surface reformation leads to (1) uniform dispersion of metal oxides on the silica surface, (2) a high Cu-Mn and Cu-Mn-Ce loading, and (3) large surface area and pore volume, all of which could be highly beneficial for $Hg^0$ adsorption and NO reduction by $NH_3$, but not thoroughly understood by previous research.

## EXPERIMENTAL SECTION

### *Preparation of Metal Oxide-incorporated Mesoporous Silica via Silicate Exfoliation*

The $CuO_x$-$MnO_x$/$SiO_2$ samples were prepared by the silicate exfoliation method with a mole ratio of the precursor metal nitrate set at (Cu + Mn)/Si = 1. Firstly, stoichiometric amounts of $Cu(NO_3)_2$ and $Mn(NO_3)_2$ were dissolved in deionized water. The mixture was then neutralized with $Na_2CO_3$ aqueous solution to form the metal template at a proper pH ≈ 10.0 followed by adding the required amounts of sodium silicate solution into the metal salt solution. Then, the mixture was stirred for 2 h at 40°C and hydrothermally treated at 100°C for 3 days. The metal oxide would reconstruct and incorporate with the silicate during the hydrothermal process. After filtration and drying, calcination at 400°C was employed for 3 h in air to yield Cu-Mn samples.

The Ce modification was conducted by adding $Ce(NO_3)_3$ (mole ratio: Ce/(Cu + Mn) = 0.1) into the Cu-Mn oxide solution in the first step. Then, the same preparation steps were followed as aforementioned to prepare Cu-Mn-Ce samples. The metal oxides were expected to completely incorporate in the $SiO_2$ samples through the silicate exfoliation method. The samples prepared with different molar ratio were denoted as CuXMnYCeZ (the mole ratio of Cu:Mn:Ce is X:Y:Z). The resulting samples were ground into powder and sieved to 40–60 mesh prior to characterization and NO/$Hg^0$ removal tests.

### *Characterization of Metal Oxide-incorporated Mesoporous Silica*

The specific surface area ($S_{BET}$) and total pore volume ($V_t$) of raw and treated samples were measured by $N_2$ adsorption at 77 K (ASAP 2020, Micromeritics). The surface morphology and particle size was observed using scanning electron microscopy (SEM; JCM-6000Plus, JEOL) and transmission electron microscopy (TEM; JEM-1400; JEOL). The crystalline structures of samples were determined with X-ray diffraction measurement (XRD; XRD-7000S, Shimadzu). The Fourier transform infrared spectroscopy (FTIR; Spectrum RX1, PerkinElmer) spectra were taken at room temperature and the spectra were recorded in the 2000–500 $cm^{-1}$ range. X-ray photoelectron spectroscopy (XPS; ESCALAB 250, VG Scientific) was employed to understand the surface chemical compositions and valence states of metal oxides on the samples. For XPS analysis, all binding energies were referenced to $C_{1s}$ peak at 285 eV. The catalytic properties of resulting samples were characterized by $H_2$ temperature-programmed reduction ($H_2$-TPR) and $NH_3$ temperature-programmed desorption ($NH_3$-TPD) experiments. In $H_2$-TPR and $NH_3$-TPD, samples were firstly pretreated in a pure Ar flow at 150°C. $H_2$-TPR experiments were conducted on a Micromeritics II Autochem 2920 by increasing the temperature to 600°C at a rate of 10 °C $min^{-1}$ with 50 mL $min^{-1}$ of 10% $H_2$/Ar. For $NH_3$-TPD experiments, samples were treated with 10% $NH_3$/Ar for 1 h and then heated up to 750°C at a heating rate of 10 °C $min^{-1}$. The amount of $NH_3$ desorption from samples was detected by the Micromeritics II Autochem 2920.

### *NO and $Hg^0$ Removal Tests*

$Hg^0$ removal performance was examined in a fixed-bed testing apparatus (Fig. 1), similar to our previous study (Chiu *et al.*, 2014), using a simulated flue gas containing 30 μg $Nm^{-3}$ $Hg^0$. $Hg^0$ was generated with a certified $Hg^0$ permeation tube (VICI Metronics) in a gas generator at specific temperature to ensure a constant $Hg^0$ diffusion rate. 12% $CO_2$, 10% $H_2O$, 6% $O_2$, 50 ppmv HCl, 200 ppmv $SO_2$, 200 ppmv NO, and balanced $N_2$ were applied as the simulated CFPP flue gas condition. The resulting gas was then passed through a temperature-controlled fixed-bed column (i.d.: 0.5″) containing 10 mg sample and 0.5 g quartz sand. The gas flow through an empty column was about 1.5 L $min^{-1}$ at 25°C. The column length of sample/sand mixture was about 1.5 cm, and the time for gas stream to

**Table 1.** Summary of studies on Cu/Mn and other metal oxide catalysts for NO and $Hg^0$ removal.

| Material | Reaction condition | Target pollutant | Experimental results | References |
|---|---|---|---|---|
| Cu-Mn oxide (molar ratio Cu/Mn = 50, 25, 1, 1/25, and 1/50) | 1. 500 ppm NO, 500 ppm $NH_3$, 5 vol.% $O_2$ balanced by $N_2$; 100 ppm $SO_2$, 11 vol.% $H_2O$ when needed<br>2. Gas hourly space velocity (GHSV): 30,000 $h^{-1}$<br>3. Tubular flow reactor of 8 mm i.d.<br>4. Temperature: 25–300°C | NO | 1. Cu0.01Mn0.25 showed the best performance at temperature range from 25 to 200°C.<br>2. Catalyst activity primarily depended on the calcination temperature which resulted in increasing pore volume and metal species in high oxidation state.<br>3. The NO conversion decreased from 95% to 64% in the presence of $SO_2$ and $H_2O$. | Kang *et al.* (2006) |
| $MnO_x$/Alumina | 1. 200–2000 ppm $SO_2$, 5 vol.% $O_2$ balanced by $N_2$; 2.4 g $MnO_x/\gamma$-$Al_2O_3$<br>2. Flow rate: 1.66 L $min^{-1}$<br>3. GHSV: 31,250 $h^{-1}$<br>4. Temperature: 100–500°C (mainly in 300–400°C region)<br>5. $Hg^0$ concentration: approximately 165 μg $m^{-3}$ (20 ppv) | $Hg^0$ | 1. The effect of NO, $CO_2$, and 0–5% $H_2O$ was not obvious on the mercury removal.<br>2. HCl enhanced the mercury oxidation. The desorption of pre-adsorbed mercury occurred in the presence of HCl; the species in the outlet was mostly $Hg^{2+}$.<br>3. $SO_2$ slightly inhibited the mercury removal in the presence of HCl and strongly decreased the $Hg^0$ adsorption ability. | Qiao *et al.* (2009) |
| CuO-$MnO_2$-$Fe_2O_3$/$\gamma$-$Al_2O_3$ (CMFA) | 1. SFG condition: 10% $CO_2$, 5% $O_2$, 400 ppm $SO_2$, 10 ppm HCl, 200 ppm NO, 8% $H_2O$ balanced by $N_2$; 0.3 g of sample<br>2. Flow rate: 1 L $min^{-1}$<br>3. GHSV: 12,800 $h^{-1}$<br>4. Temperature: 300°C<br>5. $Hg^0$ concentration: 75 μg $m^{-3}$ | $Hg^0$ | 1. $Hg^0$ concentration slightly dropped (from 75 to 55 μg $m^{-3}$) in the condition only $O_2$ and $N_2$ was purged in.<br>2. For 3-day test (in SFG condition), CMFA could adsorbed all of $Hg^{2+}$ in the beginning; $Hg^{2+}$ was first detected after 10 hours.<br>3. CMFA pre-adsorbed HCl strongly enhanced $Hg^0$ adsorption (about 95% efficiency in 120-minute test). | Wang *et al.* (2013) |
| Cu-$MnO_x$/$TiO_2$ (molar ratio Cu/Mn = 0.025, 0.05, 0.1, 0.15, and 0.2) | 1. 720 ppm NO, 800 ppm $NH_3$, 3 vol.% $O_2$ balanced by $N_2$; 8 vol.% $H_2O$ when used; 200 mg sample<br>2. GHSV: 40,000 $h^{-1}$<br>3. Tubular flow reactor of 5 mm i.d.<br>4. Temperature: 35–200°C | NO | 1. Over 95% NO conversion was shown on 0.05Cu-$MnO_x$/$TiO_2$ at 180°C for 18-hour test.<br>2. Copper improved the resistance of potassium poisoning over $MnO_2$/$TiO_2$.<br>3. $H_2O$ caused the reversible inhibition on 0.2Cu-$MnO_x$/$TiO_2$. The conversion decreased from 95% to 85%. | Fang *et al.* (2014) |
| Ce-Cu modified $V_2O_5$/$TiO_2$ based commercial SCR catalysts | 1. 500 ppm NO, 500 ppm $NH_3$, 1000 ppm $SO_2$, and 5% $O_2$ balanced by $N_2$<br>2. Flow rate: 1.5 L $min^{-1}$<br>3. GHSV: 45,000 $h^{-1}$<br>4. Temperature: 150–400°C<br>5. $Hg^0$ concentration: 30 μg $m^{-3}$ | $Hg^0$/NO | 1. 7%Ce-1%Cu/SCR showed the best removal efficiency on mercury and NO.<br>2. Commercial SCR modified with 7%Ce-1%Cu improved the SCR activity in the presence of $SO_2$ (recovery from 65% to 90%). | Chi *et al.* (2017) |

**Table 1.** *(continued).*

| Material | Reaction condition | Target pollutant | Experimental results | References |
|---|---|---|---|---|
| Cu-Mn/ordered mesoporous carbon (prepared by three different methods: self-assembly (S), ultrasound-assisted impregnation (I), and mechanical mixing (M)). | 1. 500 ppm NO, 500 ppm $NH_3$, 5% $O_2$ balanced by $N_2$<br>2. Flow rate: 0.06 L $min^{-1}$<br>3. GHSV: 36,000 $h^{-1}$<br>4. Temperature: 100–300°C | NO | 1. Cu-Mn/OMC(S) performed the highest NO conversion (88%) at 250°C.<br>2. XRD indicated manganese oxides are highly dispersed on the surface of the Cu-Mn/OMC(S).<br>3. According to XPS, the self-assembly method provided the highest ratio of $Mn^{4+}/Mn^{3+}$, $Cu^{2+}/Cu^{+}$, and chemisorbed oxygen. | Yu *et al.* (2017) |
| $MnO_x$ supported by $TiO_2$, $Al_2O_3$, $SiO_2$, and MK 10 (montmorillonite K 10) | 1. 5% $O_2$ balanced by $N_2$; 0.05 g of sample test for 10 hours<br>2. Flow rate: 0.5 L $min^{-1}$<br>3. GHSV: 478,000 $h^{-1}$<br>4. Temperature: 100–400°C<br>5. $Hg^0$ concentration: 120 μg $m^{-3}$ | $Hg^0$ | 1. The removal mechanism was divided into three parts: physical adsorption, chemical adsorption, and oxidation. Chemical adsorption was dominant at 350°C.<br>2. According to XPS, stronger electron transition between $Mn^{4+}$ and $Mn^{3+}$ (or $Mn^{3+}$ and $Mn^{2+}$) corresponded to either the adsorption or oxidation. Among four supports, MK 10 improved redox ability of Mn most. | Wu *et al.* (2018) |
| $Cu_yMn_zAl_{1-z}O_x$ mixed oxide | 1. 500 ppm NO, 500 ppm $NH_3$, 5 vol.% $O_2$ balanced by $N_2$; 100 ppm $SO_2$ when used; 150 mg of catalyst<br>2. Flow rate: 0.2 L $min^{-1}$<br>3. Tubular flow reactor of 10 mm i.d.<br>4. Temperature: 100–250°C | NO | 1. $Cu_2Mn_{0.5}Al_{0.5}O_x$ exhibited the highest NO conversion (91%) at 150°C.<br>2. Cu reduced the crystallinity of manganese oxide and increased the ratio of $Mn^{4+}/Mn^{3+}$ on the surface.<br>3. According to FTIR, NO conversion strongly depended on the quantity of Lewis acid sites. | Yan *et al.* (2018) |

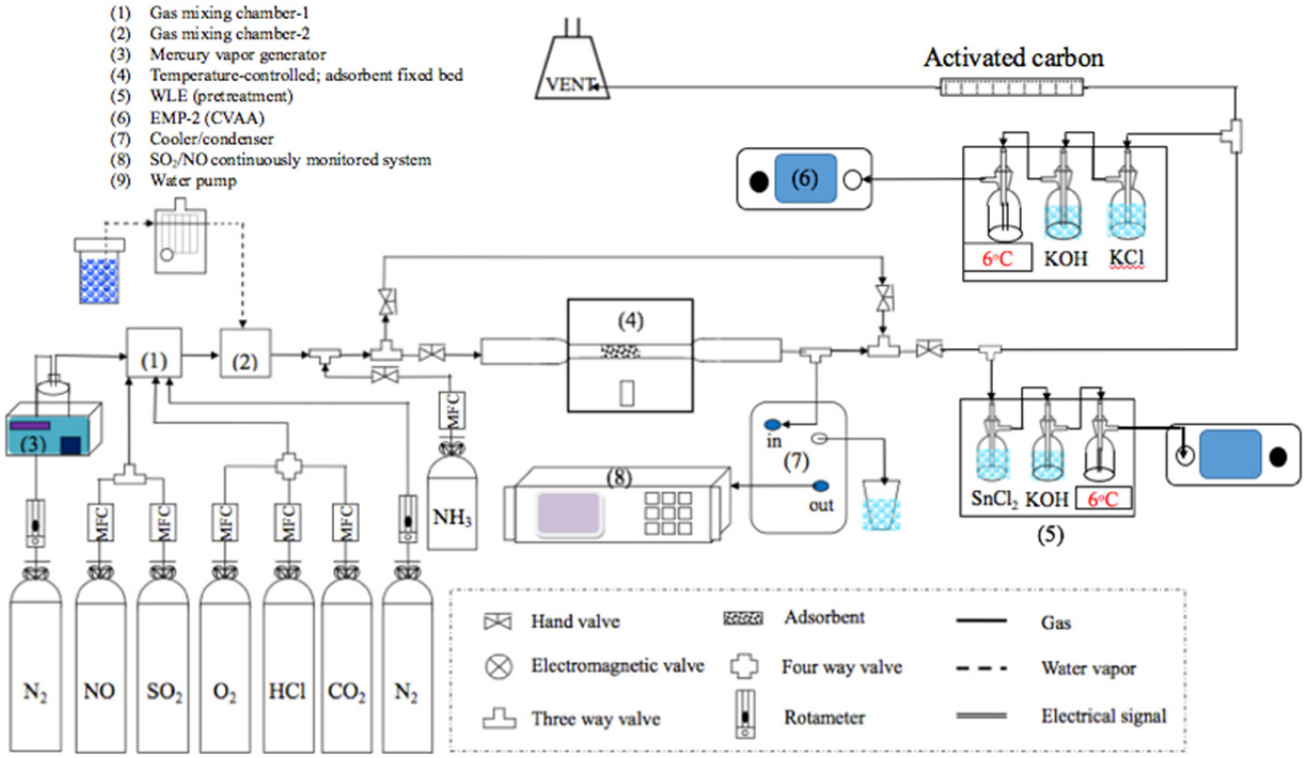


**Fig. 1.** Experimental system for fixed-bed $Hg^0$ adsorption breakthrough tests of metal oxide incorporated $SiO_2$ (Chiu *et al.*, 2014).

pass the mixture was approximately 0.08 s. The effluent gas from the fixed-bed column was heated by heating tapes and divided into two streams. One stream flowed to an impinger containing $SnCl_{2(aq)}$. $SnCl_{2(aq)}$ was applied to reduce any oxidized Hg compounds to $Hg^0$ to comprehend the adsorption effect of samples; CTHg refers to the total Hg (THg) concentration (i.e., $Hg^0$ + oxidized Hg) in the inlet or outlet stream. The other stream went through an impinger with $KCl_{(aq)}$ with an attempt to completely capture oxidized Hg to understand the oxidation effect to the outlet Hg by the samples; CHg0 represents the $Hg^0$ concentration in the inlet or outlet stream. The $Hg^0$ concentration in the two stream outlets was detected by two individual cold vapor atomic absorption spectrophotometers (CVAAS; EMP-2 coupled with SGM-8 Mercury Monitor, Nippon Instruments Corp.). The experiment was performed for 840 min or ceased when 100% breakthrough was achieved. The Hg adsorption capacities of samples were then calculated based on the breakthrough curves obtained from the CTHg experiment. By determining the difference between the $Hg^0$ concentration monitored by the two spectrophotometers (i.e., CTHg and CHg0), the amount of oxidized Hg in the outlet stream could be estimated. The normalized $Hg^0$ concentration of the THg and $Hg^0$ removal tests and the outlet oxidized Hg ratio were calculated as follows:

$$\text{Normalized } Hg^0 \text{ concentration} = \frac{CTHg_{outlet}}{CTHg_{inlet}} \text{ or } \frac{CHg0_{outlet}}{CTHg_{inlet}} \quad (1)$$

$$\text{Outlet oxidized Hg ratio} = \frac{CTHg_{outlet} - CHg0_{outlet}}{CTHg_{outlet}} \quad (2)$$

where $CTHg_{inlet}$ is the concentration of inlet $Hg^0$ (μg $Nm^{-3}$); $CTHg_{outlet}$ and $CHg0_{outlet}$ are the concentration of outlet $Hg^0$ (μg $Nm^{-3}$) detected by spectrophotometers through the $SnCl_2$ and KCl solution, respectively. Therefore, the $Hg^0$ removal efficiency through adsorption (η) could be determined:

$$\eta = 1 - \frac{CTHg_{outlet}}{CTHg_{inlet}} \quad (3)$$

NO removal tests were carried out to determine the optimal mole ratio of Cu/Mn/Ce in the metal oxide-incorporated silica for NO reduction by $NH_3$. The test condition was described as follows: 1 g of sample, 200 ppmv NO, 200 ppmv $NH_3$, 200 ppmv $SO_2$ (when used), 6% $O_2$, and balanced $N_2$ with a total gas flow rate of 1.5 L $min^{-1}$ (25°C) were used. The length of the sample/gas wool mixture in the fixed bed was approximately 5 cm, and the time for the gas flow to pass the mixture was approximately 1 s. NO concentration was continuously monitored with a SICK MAIHAK S710 gas analyzer, which could also monitor the concentration variation of $SO_2$ and $O_2$. The NO concentration at the outlet of reactor was acquired when the NO reduction achieved stability at a given temperature. Because a portion of the downstream NO was captured by the condenser located prior to the flue gas

analyzer, the NO removal efficiency was determined by:

$$\text{NO removal efficiency} = \frac{C_{NO}^{blank} - C_{NO}^{out}}{C_{NO}^{blank}} \times 100\% \quad (4)$$

where $C_{NO}^{blank}$ is the NO concentration obtained from the blank test. The blank test was performed under the simulated condition, without the presence of metal oxide-incorporated $SiO_2$. $C_{NO}^{out}$ is the NO concentration in the outlet gas stream, when the sample is in the fixed-bed reactor.

Based on our preliminary examination, Cu5Mn5, Cu2Mn8, Cu6Mn4Ce1, and Cu8Mn2Ce1 were selected for further investigation to understand the effects of temperature and presence of $SO_2$ due to their better NO removal performance within the tested Cu-Mn and Cu-Mn-Ce samples.

## RESULTS AND DISCUSSION

### *Characterization of Cu-Mn and Cu-Mn-Ce Incorporated $SiO_2$*

The XRD patterns of four samples, including Cu5Mn5, Cu2Mn8, Cu6Mn4Ce1, and Cu8Mn2Ce1 are shown in Fig. 2(a). The broad peak below 30° was denoted as amorphous silica. In addition, no crystalline phase was determined from these patterns. These results suggest that the samples may be amorphous or the metal oxides are highly dispersed on the surface of silica. The weak and broad diffraction peaks at 30.8°, 35°, 57.4°, and 62.4° were attributed to the Cu phyllosilicate in the form of $Cu_2Si_2O_5(OH)_2$ with poor crystallinity. Cu phyllosilicate is the layered structures composed of polymeric sheets of $SiO_4$ tetrahedra linked to sheets of $Cu(O,OH)_6$ octahedra, which are usually divided into 1:1 and 2:1 by layer type

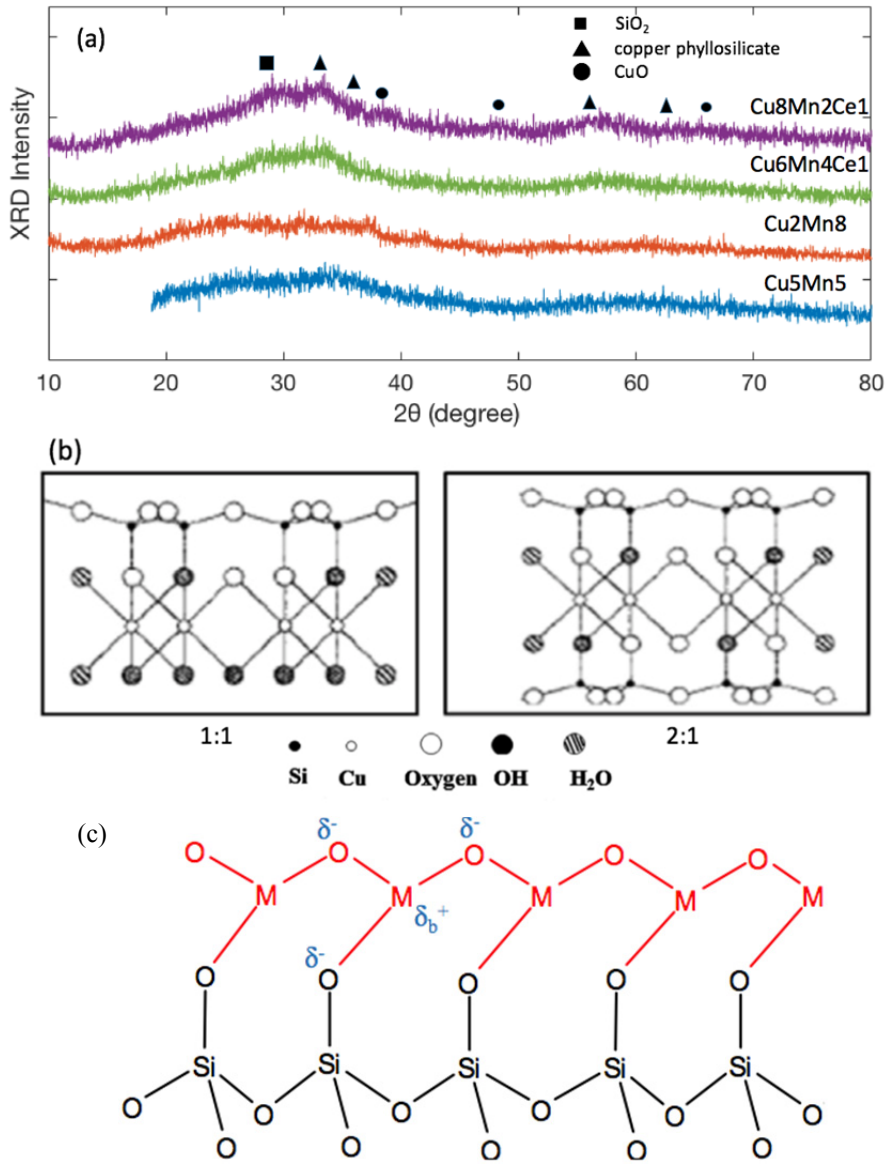


**Fig. 2.** (a) XRD patterns of metal-oxide incorporated $SiO_2$; (b) the structures of 1:1 and 2:1 copper phyllosilicate (Di *et al.*, 2016); (c) bonding structure formed in the $SiO_2$ surface by silicate-exfoliation method.

(the number of $SiO_4$ tetrahedral layers:the number of metal oxide octahedral layers; Fig. 2(b)). The existence of Cu phyllosilicate phase suggested the formation of monomer species contained Cu-O-Si bridges (Di *et al.*, 2016), which may further polymerize and construct the layer structure of Cu phyllosilicate during the hydrothermal process. Additionally, from the FTIR spectra (Fig. 3), one can clearly see that the copper silicate had a representative absorption band at 1040 $cm^{-1}$ from the Cu-O-Si stretching smaller than that of the pure silica at 1100 $cm^{-1}$ from the Si-O-Si stretching (Yue *et al.*, 2013). This decrease in wavelength indicates the formation of the Cu-O-Si bonds in the copper silicate. In this study, the presence of similar structure as described by Di *et al.* (2016) was also partly supported by the TEM images, presenting as the arrays of nano-sphere and nano-rod structures (Fig. 4), which may be formed due to the inequivalence of the constituent layer of Cu phyllosilicate (Fig. 2(c)).

Table 2 shows the textural properties of the samples based on the 77 K $N_2$ adsorption. The $S_{BET}$ of the samples was large within 378 and 602 $m^2$ $g^{-1}$, as compared to approximately 160 $m^2$ $g^{-1}$ of raw spherical $SiO_2$. The large $S_{BET}$ can be attributed to the uniform framework to form porous structure via the adequate hydrothermal synthesis instead of forming close-packed structure for Cu-Mn and Cu-Mn-Ce incorporated $SiO_2$. In addition, good dispersion of metal oxides on the silica surface helps avoiding the aggregation of metal oxides on the $SiO_2$ surface to block the pore openings. Therefore, the largest $S_{BET}$ and the arrays of nano-sphere and nano-rod structures were shown on the surface layer of Cu5Mn5 sample (Figs. 4(a), 4(b) and 5(a)), indicating that the Cu/Mn mole ratio = 1 could be the optimal condition to prepare well-dispersed Cu-Mn samples. These experimental results also suggest that the metal oxide layer may contain the Mn-O-Cu bonds to inhibit the metal oxide aggregation. In contrast, Ce oxide modification caused the decrease of $S_{BET}$ and pore volume due to the complicated interactions between these metal species, that may result in mesopore blockage, which are suggested by Figs. 4(c)–4(f), in which the original spherical $SiO_2$ particles disappeared and significant aggregation was shown. Di *et al.* (2016) also suggested that because copper phyllosilicates possess high specific surface area, the larger surface area of Cu-Mn samples may be attributed to more copper phyllosilicates, or special type of copper phyllosilicate species preserved in the samples.

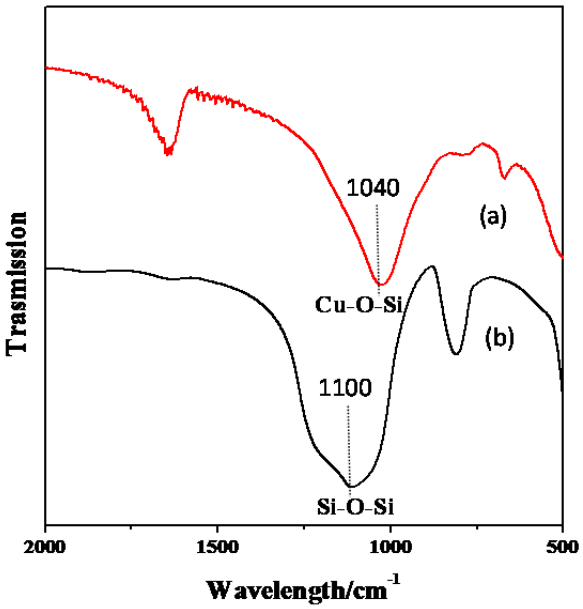


**Fig. 3.** FTIR spectra of the (a) Cu-incorporated silicate and (b) pure silica.

Fig. 6 shows the $H_2$-TPR profiles of Cu-Mn and Cu-Mn-Ce samples. Single metal oxide samples, namely Cu- and Mn-silicates, were also prepared and examined for comparison. The reduction peak centered at 225°C for the Cu-silicate was attributed to two reasons: (1) one-step reduction of low interacting species $Cu^{2+}$ to $Cu^0$, and (2) partial reduction of highly dispersed species ($Cu^{2+} \rightarrow Cu^+$) (Diaz *et al.*, 1999). However, as described by Shi *et al.* (2018), $Cu^{2+}$ to $Cu^0$ may not likely occur at our experimental condition. There were two reduction peaks over the Mn-silicate: The peaks under 300°C and above 300°C could be denoted as $MnO_x$ species to $Mn_3O_4$ and $Mn_3O_4$ to MnO, respectively (Shi *et al.*, 2018; Yi *et al.*, 2018). Different from Cu- and Mn-silicate, the broad reduction peak was observed in the results of Cu-Mn samples (except for Cu2Mn8). Yan *et al.* (2018) proposed that the broad reduction was caused by the synergistic effect, which was related to the electron transfer between Cu and Mn oxides. Furthermore, the trimodal peaks observed over the Cu2Mn8 sample indicated less Cu-Mn interaction on its surface.

$NH_3$-TPD was carried out to characterize the surface acidity and $NH_3$ adsorption ability (Fig. 7). The desorption peak of Cu5Mn5 at 100°C was denoted as the physically adsorbed $NH_3$. Zheng *et al.* (2013) proposed that the $NH_3$ desorption peak centered at low temperature (< 400°C) and the peak at high temperature (> 600°C) was assigned to weak acid sites and strong acid sites, respectively. All four samples exhibited the broad peak from 150 to 500°C, ascribed to the multiple desorption $NH_4^+$ bound to weak or strong Brønsted acid sites. Different from samples with the addition of Ce, weak desorption peak centered at 600°C originated from Lewis acid sites was observed in the results of Cu5Mn5 and Cu2Mn8. Cu6Mn4Ce1 and Cu2Mn8Ce1 had the similar $NH_3$ desorption profile, which was probably related to the corresponding redox properties and texture. The amounts of desorbed $NH_3$ (without counting the physisorbed $NH_3$) over the four samples followed the sequence: Cu2Mn8 (1.00) > Cu6Mn4Ce1 (0.89) > Cu8Mn2Ce1 (0.68) > Cu5Mn5 (0.52). The reason causing the greatest $NH_3$ adsorption capacity over Cu2Mn8 may be due to the less synergistic effect aforementioned, which influences the surface acid strength. The $NH_3$-TPD results also suggest that Ce could promote the $NH_3$ adsorption capacity, which may be mainly caused by increasing the Brønsted acid sites.

To identify the chemical state of surface species, XPS analysis was carried out over the Cu5Mn5, Cu2Mn8, Cu6Mn4Ce1, and Cu8Mn2Ce1 samples (Figs. 8(a) and 8(b)).

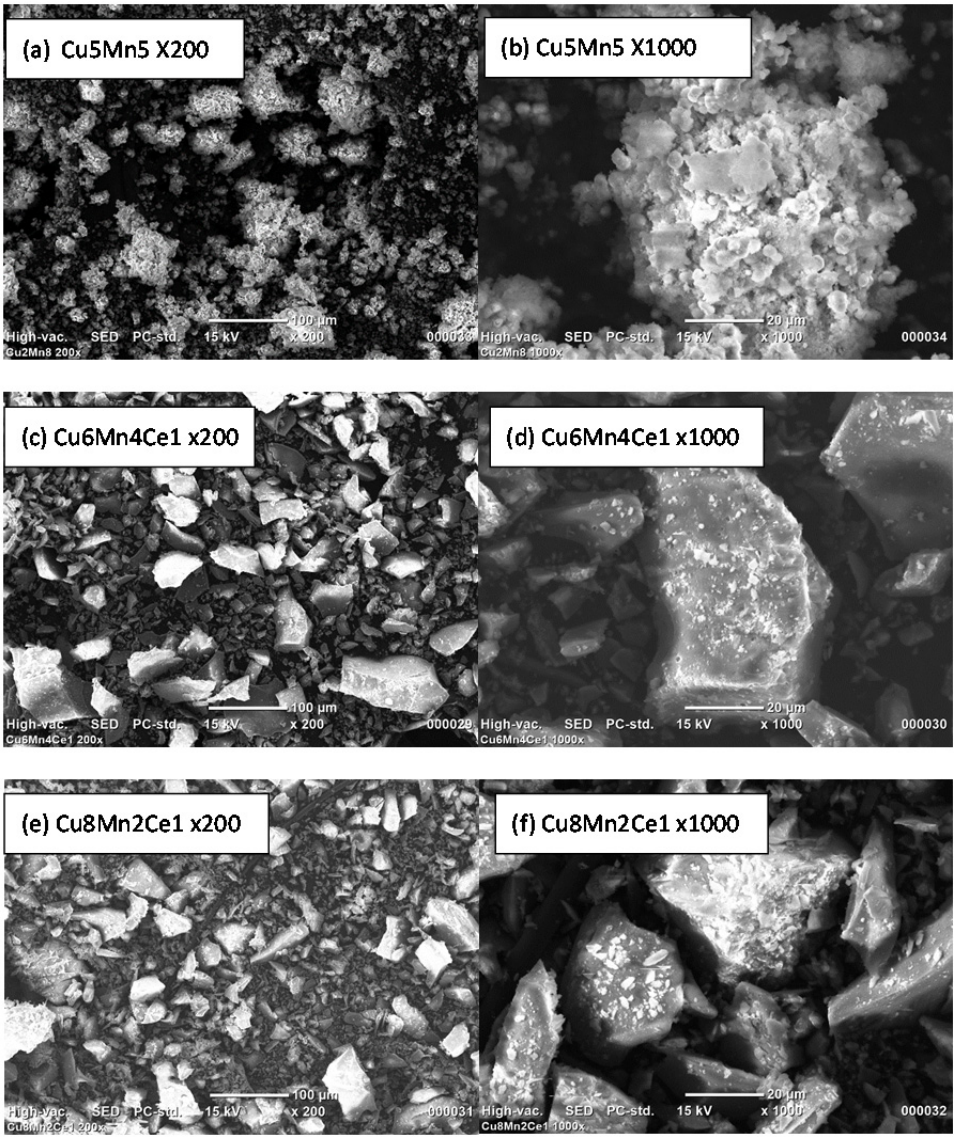


**Fig. 4.** SEM images of the Cu-Mn and Cu-Mn-Ce incorporated silica: (a) Cu5Mn5 × 200; (b) Cu5Mn5 × 1000; (c) Cu6Mn4Ce1 × 200; (d) Cu6Mn4Ce1 × 1000; (e) Cu8Mn2Ce1 × 200; (f) Cu8Mn2Ce1 × 1000.

**Table 2.** Specific surface area and pore characteristics of metal oxide-incorporated mesoporous silica.

| Sample | $S_{BET}$ ($m^2$ $g^{-1}$) | $V_t$ ($cm^3$ $g^{-1}$) | Average pore size (nm) |
|---|---|---|---|
| Cu5Mn5 | 602.2 | 0.370 | 2.455 |
| Cu2Mn8 | 384.4 | 0.377 | 3.925 |
| Cu8Mn2Ce1 | 366.4 | 0.246 | 2.686 |
| Cu6Mn4Ce1 | 378.6 | 0.260 | 2.753 |

The peaks with binding energies corresponding to Cu2p and Mn2p were further deconvoluted. The XPS spectra of Cu2p3/2 could be divided into the $Cu^+$ and $Cu^{2+}$ peaks at the binding energy of 932.8 and 934.4 eV (Yi *et al.*, 2018) (Fig. 8(a)). According to Fang *et al.* (2014), Mn2p3/2 could be separated into $Mn^{3+}$ peak at 641.8–642.0 eV, and $Mn^{4+}$ peak at 643.2–644.5 eV (Fig. 8(b)). The relative atomic concentration ratios of species are presented in Table 3. For Cu2p XPS results, greater $Cu^+$ ratios were observed in the spectra of Cu5Mn5 and Cu2Mn8; large $Mn^{4+}/Mn^{3+}$ ratios were observed in the deconvolution results of all samples (Table 3). These experimental results are attributed to the electron transfer between Cu and Mn oxides, which caused the valence transition between $Cu^{2+}$ and $Mn^{3+}$.

The XPS spectra of O1s and Ce3d were also analyzed (Figs. 8(c) and 8(d)). There were three different O species on the sample surface: the lattice oxygen (labeled as $O_\alpha$) at 529.3–530 eV, chemisorbed oxygen (labeled as $O_\beta$) at 531.2–532 eV, and hydroxyl groups, defect oxide, and adsorbed water species (labeled as $O_\gamma$) near 540 eV. In

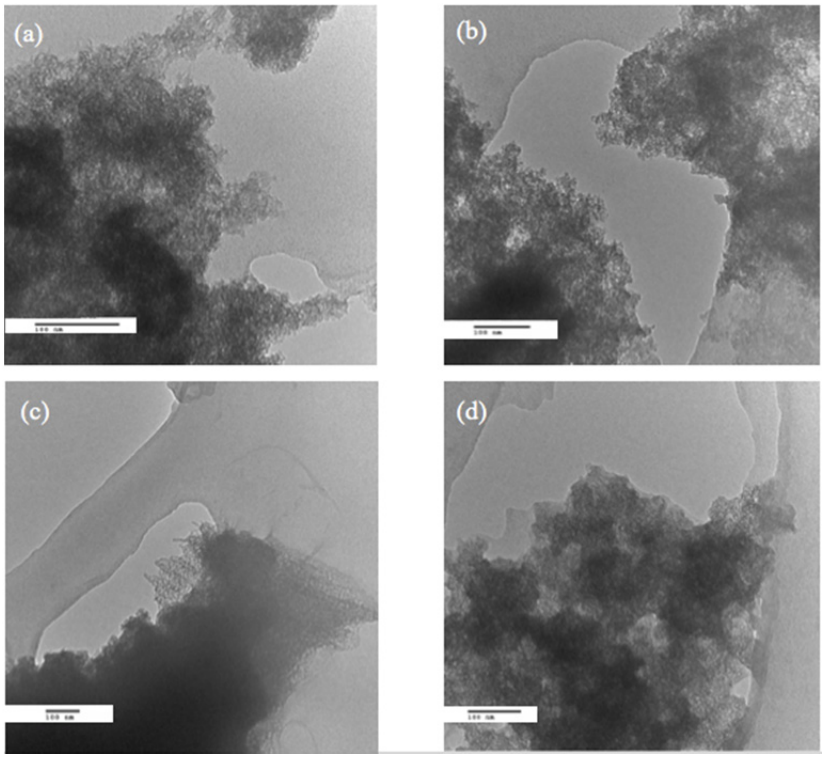


**Fig. 5.** TEM images of the Cu-Mn and Cu-Mn-Ce incorporated silica: (a) Cu5Mn5; (b) Cu2Mn8; (c) Cu8Mn2Ce1; (d) Cu6Mn4Ce1.

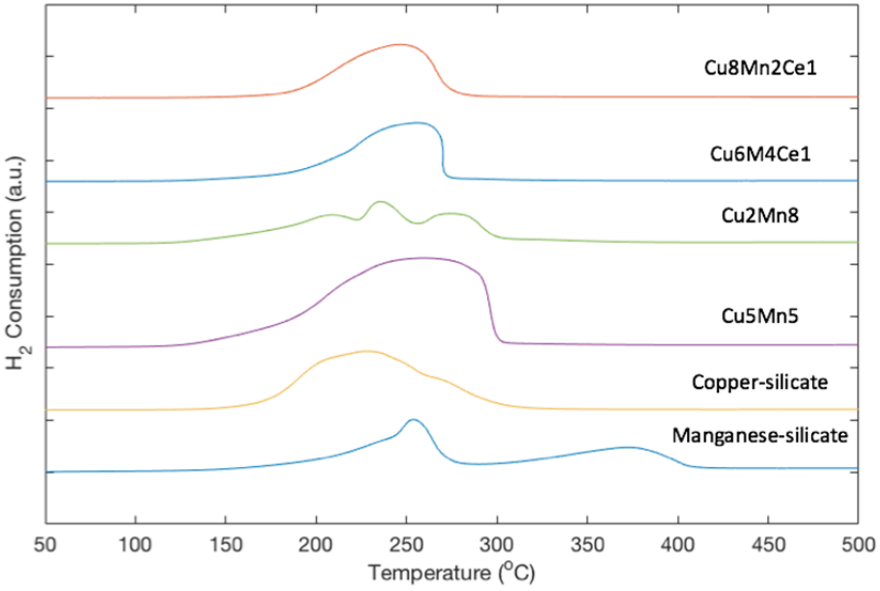


**Fig. 6.** $H_2$-TPR profiles of Cu-Mn and Cu-Mn-Ce incorporated $SiO_2$.

addition, the complex spectra of Ce3d could be divided into two different Ce cations. The subbands at 886 eV corresponded to $Ce^{3+}$; those at 901.5, 907, and 917 eV were attributed to $Ce^{4+}$. The chemisorbed oxygen was considered as a significant species in the catalytic processes (Yan *et al.*, 2018). Cations with high oxidation state ($Ce^{4+}$) give rise to a reactive ammonia complex to react with NO (Tang *et al.*, 2016); it resulted in the larger activity over the Cu6Mn4Ce1 compared with the performance over Cu8Mn2Ce1. In addition, the possible reason of high $Cu^{2+}$/Cu ratio over the Cu8Mn2Ce1 was the valence transition between $Ce^{4+}$ and $Ce^{3+}$.

### *NO Removal Activity of Cu-Mn and Cu-Mn-Ce Samples*

The NO removal performance of Cu-Mn samples is presented in Fig. 9. Without the presence of Cu oxide, Mn-silicate showed great activity at the temperature range of 200–300°C, with a NO conversion over 90%. However,

the NO removal efficiency sharply decreased to 60% with the incorporation of Cu oxides. Corresponding to the $H_2$-TPR, the incorporation of Cu oxide appeared to change the redox properties of Mn-silicate, which caused the inhibition of the SCR activity. Therefore, the greater performance over Cu2Mn8 as compared to other Cu-Mn and Cu-Mn-Ce incorporated silica may be due to a lesser influence of the synergistic effect on its Mn-based active sites.

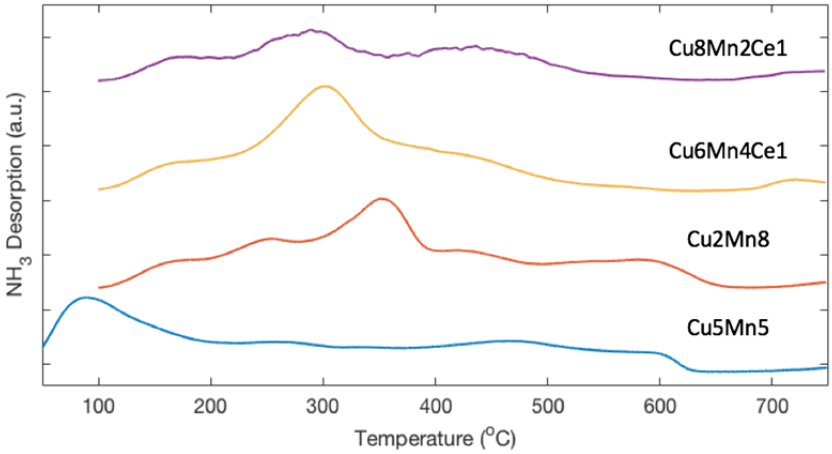


**Fig. 7.** $NH_3$-TPD profiles of Cu-Mn and Cu-Mn-Ce incorporated $SiO_2$ samples.

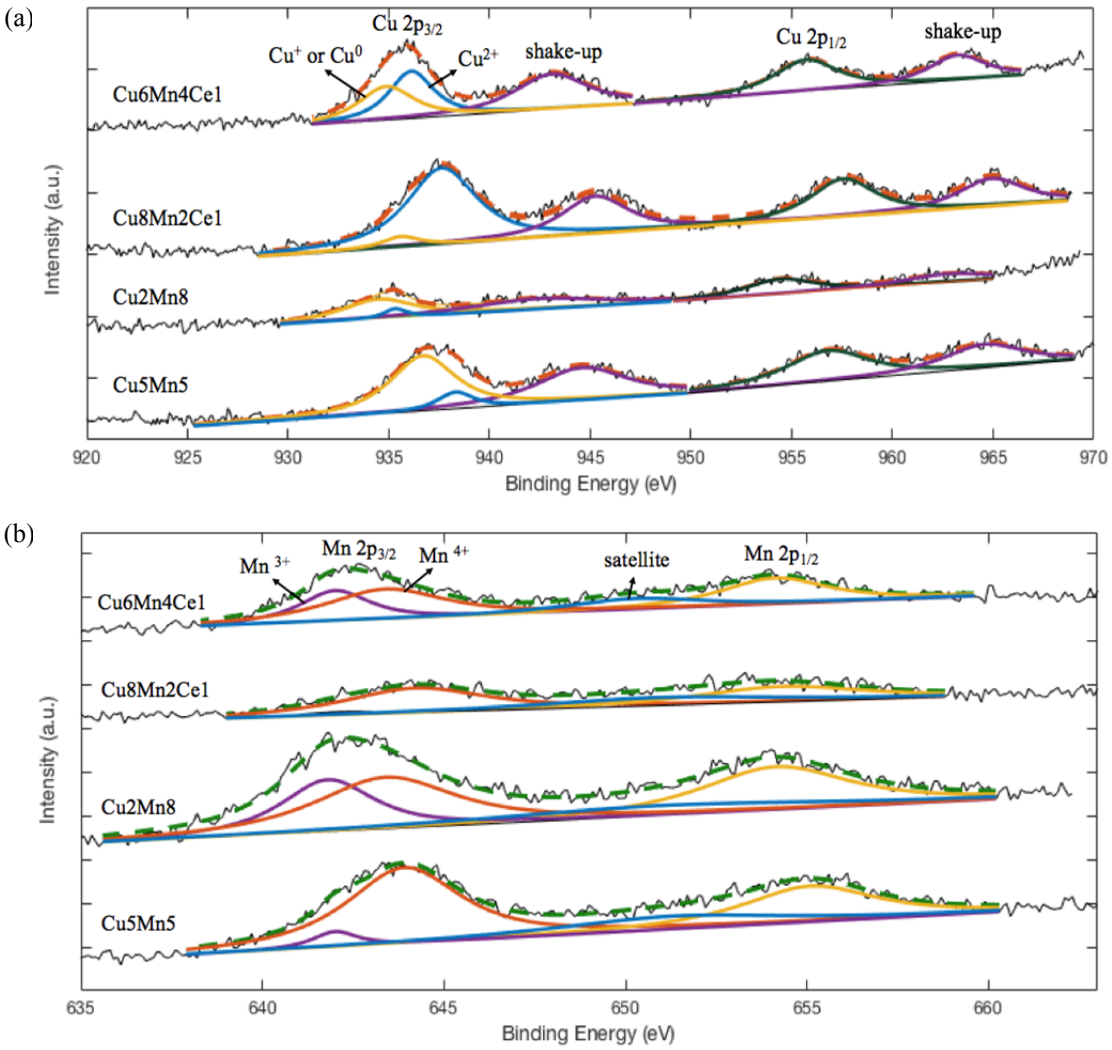


**Fig. 8.** (a) Cu2p; (b) Mn2p; (c) O1s; (d) Ce3d XPS spectra of Cu5Mn5, Cu2Mn8, Cu8Mn2Ce1, and Cu6Mn4Ce1 samples.

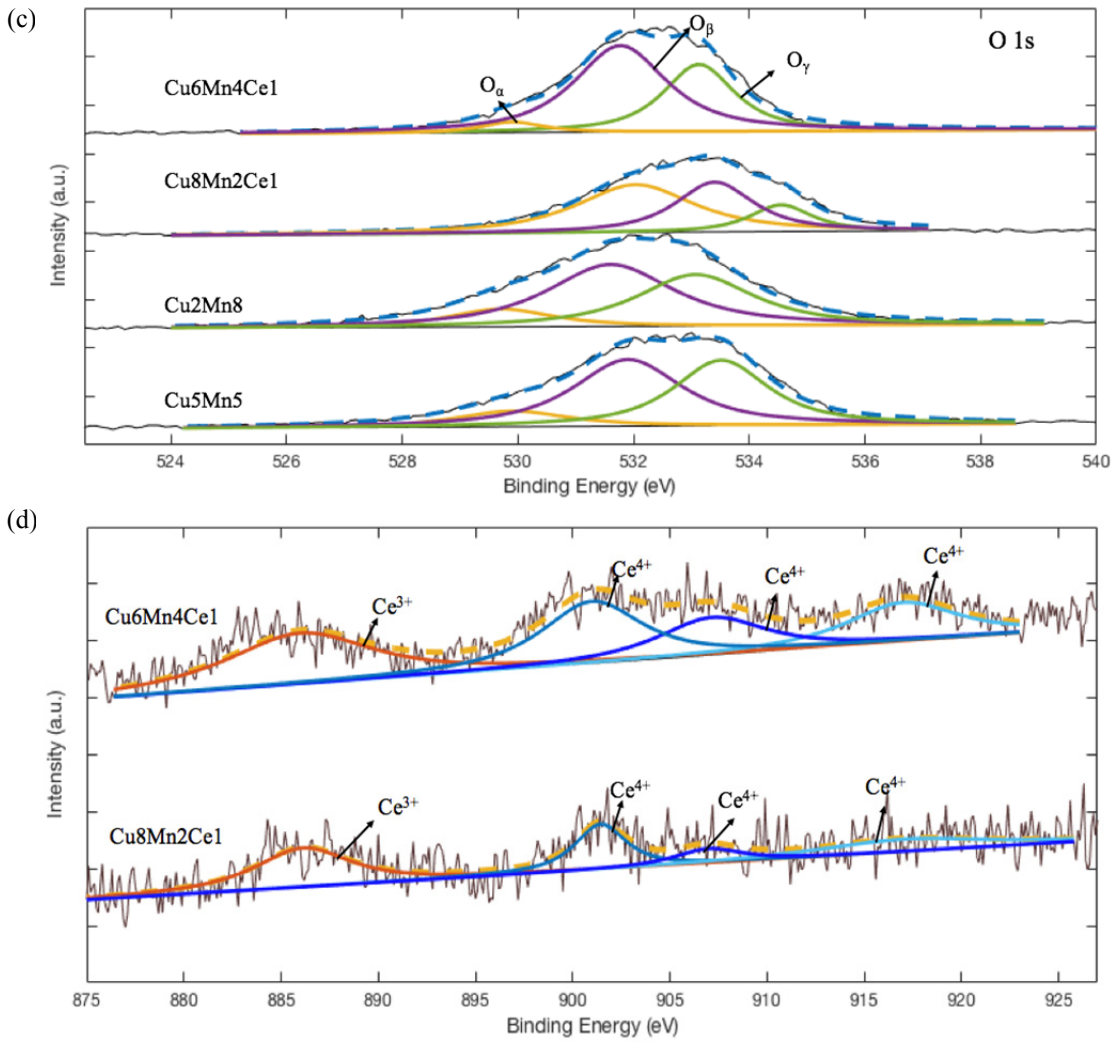


**Fig. 8.** (*continued*).

**Table 3.** The relative concentration ratios of specific states of the surface elements on the Cu-Mn-incorporated mesoporous silica.

| Sample | Relative concentration ratios (%) | | | | | |
|---|---|---|---|---|---|---|
| | $Cu^{2+}/Cu$ | $Mn^{4+}/Mn$ | $O_\alpha/O$ | $O_\beta/O$ | $O_\gamma/O$ | $Ce^{4+}/Ce^{3+}$ |
| Cu5Mn5 | 0.141 | 0.926 | 0.166 | 0.478 | 0.406 | - |
| Cu2Mn8 | 0.122 | 0.600 | 0.120 | 0.500 | 0.380 | - |
| Cu8Mn2Ce1 | 0.935 | 0.923 | 0.503 | 0.350 | 0.147 | 1.443 |
| Cu6Mn4Ce1 | 0.535 | 0.628 | 0.049 | 0.595 | 0.356 | 1.962 |

The $NH_3$ adsorption capacity of Cu6Mn4Ce1 was similar with that for Cu2Mn8 based on the $NH_3$-TPD results. It is because the high ratio of $Ce^{4+}$ coordinates with $NH_3$. It was reported that $SO_2$ would occupy the acid sites on the catalyst causing poisoning (Wei *et al.*, 2016); the addition of Ce could trap the sulfation of the active sites (Jin *et al.*, 2014). In order to understand the effect of Ce on limiting $SO_2$ poisoning, Cu2Mn8 and Cu6Mn4Ce1 having large $NH_3$ adsorption ability were selected to evaluate the NO removal efficiency at the temperature range from 150 to 350°C with presence of 200 ppmv $SO_2$ (Fig. 10). The obvious inhibition in NO reduction by $SO_2$ (i.e., 30% decrease in NO removal) was shown over Cu2Mn8. On contrary, there were no obvious decrease in NO removal for Cu6Mn4Ce1; instead, the removal efficiency at 250–350°C was further enhanced. As reported by Jin *et al.* (2014), the Ce modification causes more Brønsted acid sites, which attribute to the promotion of the SCR performance at 250–350°C. Yang *et al.* (2013) also showed that $CeO_2$ had an excellent SCR activity in the presence of $SO_2$ at 300–500°C. The promotion of $SO_2$ on the SCR reaction over $CeO_2$ was mainly due to the sulfation of $CeO_2$, which could be the reason for the promotion of NO removal by Cu6Mn4Ce1.

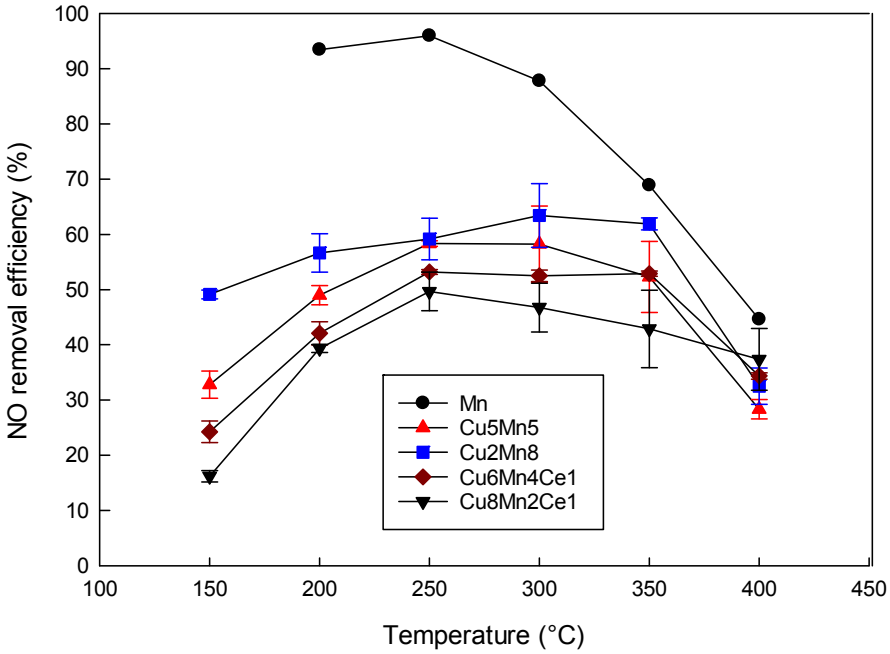


**Fig. 9.** NO removal efficiency of Cu-Mn incorporated samples as compared to Mn-silicate.

***$Hg^0$ Removal Test on Cu-Mn and Cu-Mn-Ce Incorporated Silica***

Fig. 11(a) shows the results of THg and $Hg^0$ removal tests over Cu2Mn8 under the baseline condition (i.e., at $Hg^0$ = 30 μg $m^{-3}$ and 150°C). There was no noticeable difference between CTHg and CHg0 for the 14-h test. The similar results also showed in other three samples, including Cu5Mn5, Cu6Mn4Ce1, and Cu8Mn2Ce1. These experimental results suggest that either the $Hg^0$ catalytic oxidation are not obvious on the sample surface, or, more likely, the oxidized Hg is immediately captured on the surface of the Cu-Mn and Cu-Mn-Ce silica samples. Consequently, the $Hg^0$ removal is primarily dependent on the oxidation followed by immediate adsorption. Furthermore, the experimental results also showed that 100% breakthrough was hardly achieved, which may be due to the poor adsorption kinetics between Hg and the tested samples.

For data comparison, the Hg removal performance was presented as the average THg removal efficiency and the Hg adsorption capacity over 14 h (Fig. 11(b)). The deviation represented the variation of the removal efficiency over the test. The average THg removal efficiency is determined by:

$$\text{Average THg removal efficiency} = \frac{CTHg_{inlet} - CTHg_{outlet,average}}{CTHg_{inlet}} \times 100\% \quad (4)$$

where $CTHg_{outlet,average}$ is the average $Hg^0$ concentration at the outlet over the THg test. The experimental results for Cu2Mn8 had the greatest average THg removal efficiency, indicating that the effect of Ce modification on enhancing $Hg^0$ adsorption was less significant when Mn was present in a great amount. Notably, Cu6Mn4Ce1 and Cu8Mn2Ce1 had greater average THg removal than Cu5Mn5, indicating that Ce modification enhanced $Hg^0$ adsorption when Mn was present in a smaller amount. Furthermore, the $Hg^0$ adsorption capacity of the tested samples decreased in the same order of acid site content obtained from $NH_3$-TPD data: Cu2Mn8 > Cu6Mn4Ce1 > Cu8Mn2Ce1 > Cu5Mn5. These results, in agreement with previous studies (Chang *et al.*, 2015; Liu *et al.*, 2017), suggest that the amount of the acid sites verified by $NH_3$ adsorption plays an important role in $Hg^0$ oxidation and removal. These results also suggest that the extent of surface area and pore volume should not be the determining factor on $Hg^0$ removal for the tested metal-oxide silica.

Because of its greater NO and $Hg^0$ removal performance as compared to the others, Cu2Mn8 was further tested to evaluate the effect of temperature and inlet concentration on the $Hg^0$ adsorption. The test temperatures were set at 150, 250, and 350°C and the experimental results are shown in Fig. 12(a). Again, the effect of the catalytic oxidation over Cu2Mn8 was not obviously shown in the outlet stream even at 350°C, implying that if Hg oxidation occurs on the surface of Cu-Mn silica, the oxidized Hg would be immediately adsorbed. The average $Hg^0$ removal efficiency decreased with the increase of the temperature. The decrease in THg removal efficiency at 350°C was expected because the adsorption of Hg is thermodynamically unfavorable at elevated temperature (Chiu *et al.*, 2015).

The effect of concentration on Hg adsorption over Cu2Mn8 was investigated in the similar gas condition at three inlet $Hg^0$ concentrations: 30, 65, and 100 μg $m^{-3}$ at 150°C (Fig. 12(b)). Again, oxidized Hg was not observed in the outlet stream even as the inlet $Hg^0$ was at 100 μg $m^{-3}$. The greatest THg removal efficiency was observed when the inlet $Hg^0$ increased to 65 μg $m^{-3}$. The largest adsorption capacity was obtained when the inlet $Hg^0$ concentration increased to 100 μg $m^{-3}$.

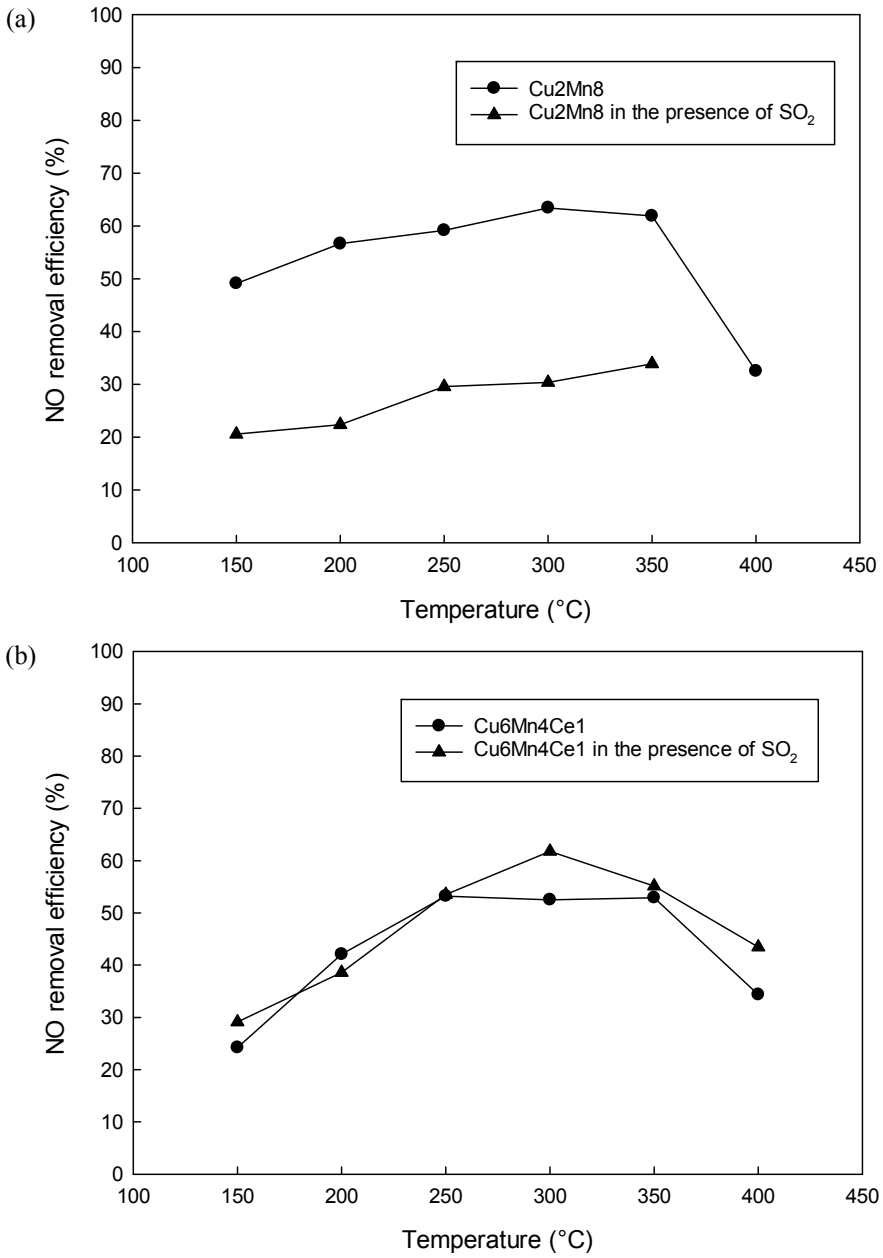


**Fig. 10.** Effect of $SO_2$ on the NO removal efficiency for (a) Cu2Mn8 and (b) Cu6Mn4Ce1.

Because of the complex composition of the simulated coal-combustion flue gas, the transient response test was further performed on Cu2Mn8 to investigate the effect of flue gas components on $Hg^0$ adsorption at 150°C. Fig. 13(a) shows the effect of pure $N_2$, 6% $O_2$, 12% $CO_2$, and 200 ppmv NO on $Hg^0$ adsorption. Firstly, there was only 10% THg removal efficiency for Cu2Mn8 in pure $N_2$ condition. It is related to the reaction of $Hg^0$ with a limited amount of lattice oxygen, which may follow the Mars-Massen mechanism (Qiao *et al.*, 2009). $Hg^0$ firstly adsorbed on the surface to form $Hg^0_{(ad)}$. The $Hg^0_{(ad)}$ then bonded with the lattice oxygen on the samples to form $HgO_{(ad)}$. The uptake of the lattice oxygen by Hg would be compensated by chemisorbed oxygen due to the high mobility.

With the addition of 6% $O_2$ at 4.5 h, the $Hg^0$ removal efficiency increased slightly (Fig. 13(a)) because the gas-phase oxygen would replenish the uptake of the lattice oxygen and chemisorbed oxygen. At around 5.8 h, 12% $CO_2$ was introduced and there was no significant difference. Then, 200 ppmv NO was added in at 6 h. The THg removal efficiency increased to 25% and small amount of oxidized Hg was observed at the outlet. NO could be adsorbed on the basic sites of metal-oxide catalysts and give rise to active species, such as $NO_2$ and $NO_2^+$ for Hg oxidation. Li *et al.* (2011b) also suggested the oxidized Hg detected at the outlet was some volatile mercuric compounds, such as $Hg(NO_3)_2$.

Following the test, 50 ppmv HCl was added in at 9 h (Fig. 13(a)). The THg and $Hg^0$ removal efficiency sharply increased to 80 and 95%, respectively. The high Hg

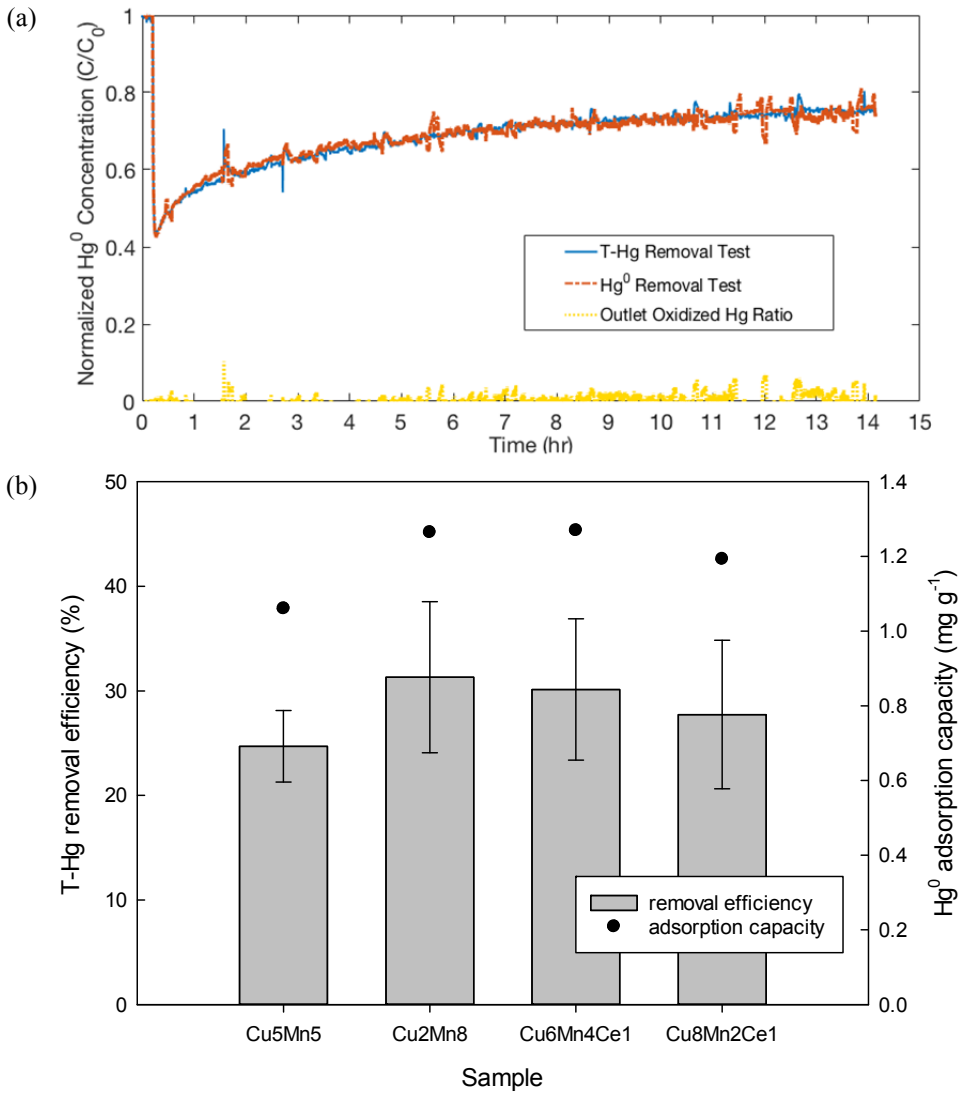


**Fig. 11.** (a) Results of THg and $Hg^0$ removal tests for Cu2Mn8. (b) The average THg removal efficiencies and adsorption capacity over 14-h test for samples at 150°C.

oxidation by HCl, which may stem from formation of $HgCl_2$, has been proposed by several studies (Presto and Granite, 2006; Wang *et al.*, 2014). Therefore, further investigation for better understanding the enhancing behavior of $Hg^0$ adsorption by HCl at 150°C was done on Cu2Mn8, shown in Fig. 13(b). Firstly, the Cu2Mn8 sample was pretreated with 50 ppmv HCl for 1 h and purged with $N_2$ for 0.5 h; then, 30 μg $m^{-3}$ $Hg^0$ carried by $N_2$ was applied to the HCl-pretreated sample. The THg removal efficiency was shown to slowly decrease from 55 to 35% for 7 h. Consequently, HCl was confirmed to be strongly adsorbed on the surface of Cu2Mn8 and further oxidized and captured $Hg^0$. At 7 h, the addition of oxygen, as mentioned above, replenished the deficiency of the surface oxygen that further enhanced the $Hg^0$ adsorption again.

According to the transient response and HCl pretreatment test, the adsorbed HCl is confirmed to play the dominant role in the $Hg^0$ oxidation/adsorption over the Cu-Mn samples. HCl would be adsorbed on the surface through two pathways (He *et al.*, 2009; Chang *et al.*, 2015): (1) The adsorbed HCl on the original basic sites of Cu-Mn samples would modify the chemical environments of samples, which caused the shift of the valence due to the strong electronegativity of Cl (Eq. (5)), and (2) the adsorbed HCl could bond with neighboring sites (Eq. (6)).

$$M^{(n-1)+} - OH + Cl^- \rightarrow Cl - M^{n+} - OH \quad (5)$$

$$M^{n+} = O + HCl \rightarrow Cl - M^{n+} - OH \quad (6)$$

where M could be Mn or Cu in this study.

Based on the aforementioned results, the $Hg^0$ removal mechanism may be explained by the Langmuir-Hinshelwood mechanism:

$$HCl + 4Mn^{4+}{=}O \rightarrow Cl\text{-}Mn^{4+} - OH \quad (7)$$

$$Cl^- + Cu^+ - OH \rightarrow Cl\text{-}Cu^{2+} - OH \quad (8)$$

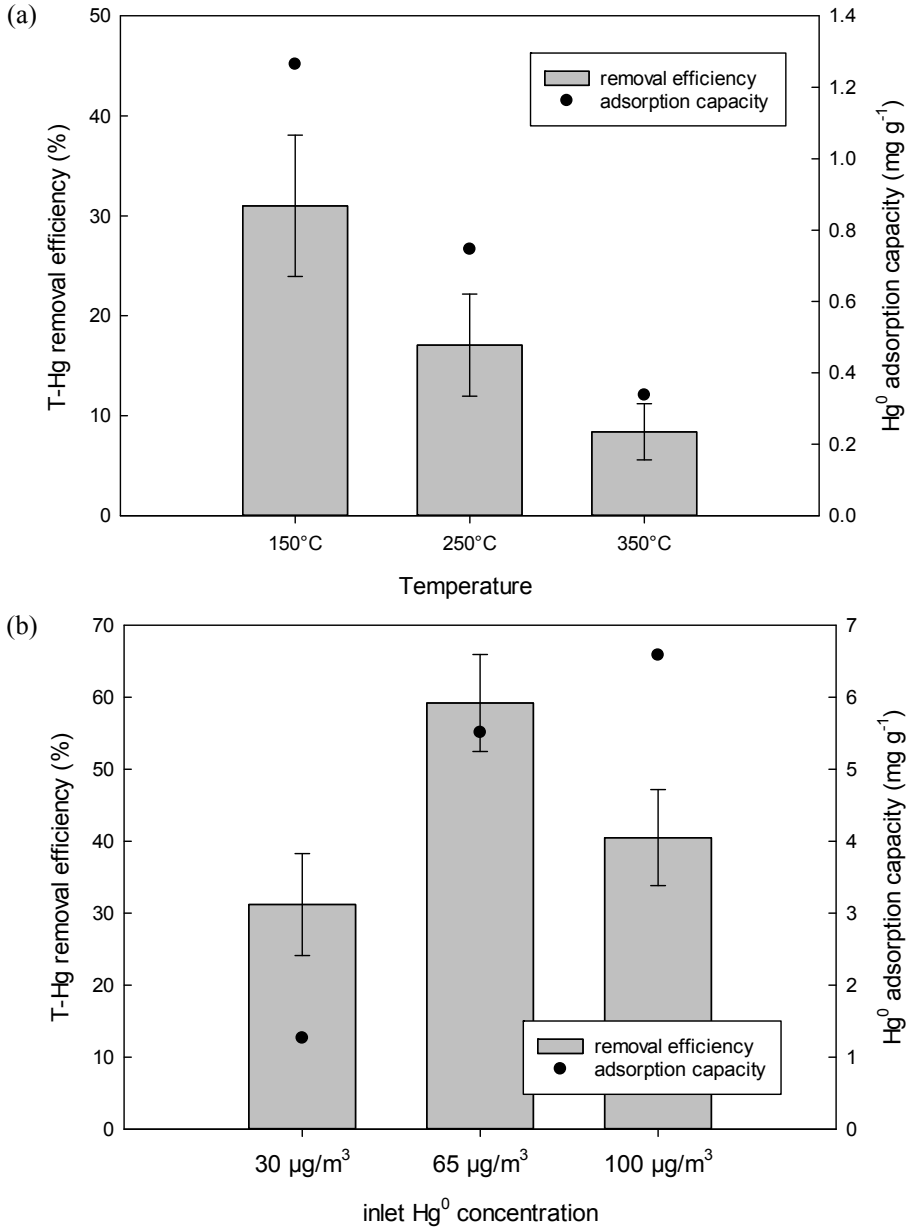


**Fig. 12.** (a) Temperature dependence of average THg removal efficiency and the adsorption capacity with the inlet $Hg^0$ concentration of 30 μg $m^{-3}$ for Cu2Mn8. (b) Concentration dependence of average THg removal efficiency and the adsorption capacity at 150°C for Cu2Mn8.

$$Hg + Mn^{4+}=O \rightarrow Mn^{4+} - O - Hg \quad (9)$$

$$Mn^{4+} - O - Hg + Cl\text{-}Cu^{2+} - OH \rightarrow Mn^{4+} - O - HgCl + Cu^{+} - OH \quad (10)$$

$$Mn^{4+} - O - HgCl + Cl\text{-}Mn^{4+} - OH \rightarrow HgCl_2 + Mn^{4+}=O + Mn^{3+} - OH \quad (11)$$

$$Mn^{3+} - OH + 1/4O_2 \rightarrow Mn^{4+}=O + 1/2H_2O \quad (12)$$

Because of a low energy barrier in the reaction between Hg and Cl, the probable reactions would occur between reactive Cl and $Hg^0$ on the surface of samples (Presto and Granite, 2006). First, HCl would adsorb on the surface basic sites and generate the reactive Cl. The low ratios of $Cu^{2+}$/Cu and high ratios of $Mn^{4+}$/Mn in the XPS results indicate that the probable sites are $Cu^{+}$, which is activated by the reactive Cl, and $Mn^{4+}$ would bond with HCl. Furthermore, the correspondence between the results of the $NH_3$-TPD and the $Hg^0$ removal test suggest that the acid sites, both the Brønsted and Lewis acid sites, could be the activated Cl species. Then, the adsorbed $Hg^0$ would react with the reactive Cl to form $HgCl_2$, which is quickly adsorbed by the samples. The reoxidation of the $Mn^{3+}$–OH species by oxygen replenishes $Mn^{4+}$=O. Notably, $Hg^0$ oxidation may also follow the Eley-Rideal mechanism (Xiong *et al.*, 2017), for which gaseous $Hg^0$ directly reacts with the adsorbed reactive Cl to form $HgCl_2$ and the formed $HgCl_2$

are mostly released back to the gas phase and leads to significant $Hg^0$ oxidation in the outlet stream. This may not be the case observed in our experiments because most of the formed oxidized Hg are speculated to adsorb on the sample surface.

The transient response test implied that the THg removal efficiency could achieve over 95% with the flue gas condition without the presence of $SO_2$ and $H_2O$ vapor. Therefore, the effect of $SO_2$ was further investigated (Fig. 14). The results showed that the $Hg^0$ oxidation kept over 90%, but the Hg capture efficiency gradually decreased from 80 to 60%. These experimental results indicate that the competitive

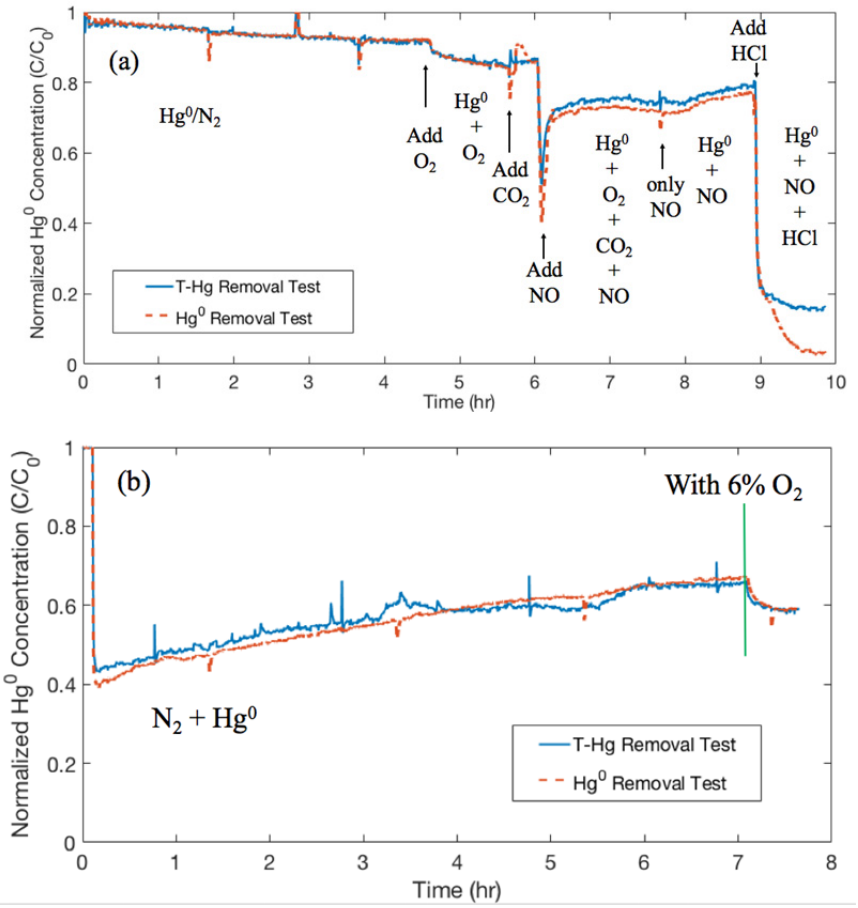


**Fig. 13.** (a) Transient response test on Cu2Mn8 sample. (b) $Hg^0$ adsorption and oxidation test for Cu2Mn8 pretreated with 50 ppmv HCl.

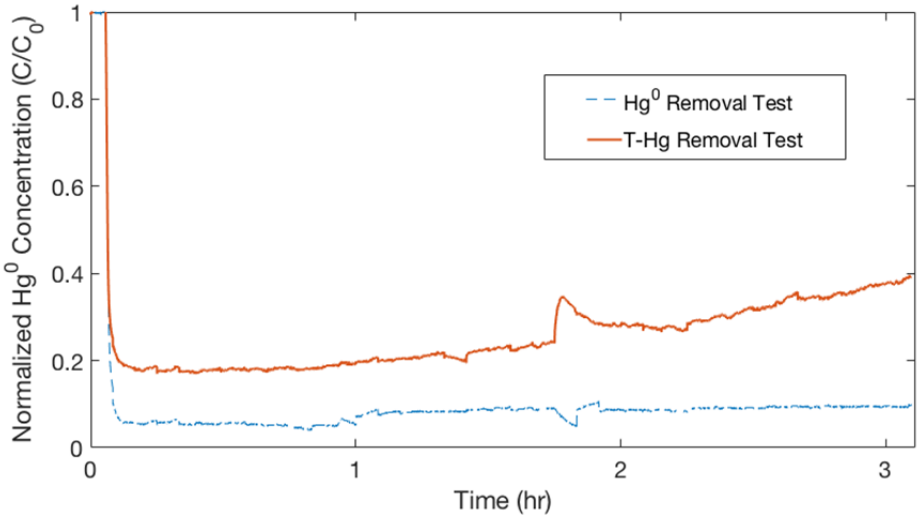


**Fig. 14.** Effect of 200 ppmv $SO_2$ on $Hg^0$ oxidation and adsorption for Cu2Mn8 sample.

adsorption between the possibly formed $HgCl_2$ and $SO_2$ did not inhibit the $Hg^0$ oxidation, but the oxidized Hg is less adsorptive, and a portion of it is released into the outlet stream. $H_2O$ has also been reported to inhibit $Hg^0$ oxidation and removal over metal or metal oxide based catalysts due to the competitive adsorption with reactive species, which caused the decrease of the overall $Hg^0$ oxidation efficiency (Li *et al.*, 2011b).

## CONCLUSIONS

We hydrothermally exfoliated silicate to create mesoporous $SiO_2$ with a large specific surface area and well-dispersed Cu-Mn and Cu-Mn-Ce oxides. The presence of Cu phyllosilicate, detected via XRD, in the $SiO_2$ indicated that the constituent layer contained Cu-O-Si bonds that had formed during the exfoliation, resulting in the formation of nano-sphere and nano-rod structures, which were observed in TEM images. The transfer of valences between $Cu^{2+}$ and $Mn^{3+}$ led to the single reduction peak displayed in the TPR profiles and the high $Mn^{4+}$/Mn and $Cu^{+}$/Cu ratios observed via XPS. Synergistic effects inhibited the NO removal efficiency of the Cu-Mn silica. However, incorporating Ce enhanced the catalyst's resistance to $SO_2$ poisoning and increased its adsorption of $NH_3$, thereby promoting the reduction of NO. $Hg^0$ was primarily removed via adsorption for the Cu-Mn as well as the Cu-Mn-Ce silica. Based on transient response experiments, the main reactions occurred between the adsorbed HCl and the surface of the silica, resulting in the formation of reactive Cl, which led to the oxidation, followed by the immediate adsorption, of $Hg^0$.

## ACKNOWLEDGMENTS

This study was financially supported by the Ministry of Science and Technology of Taiwan (MOST 103-2622-E-002-038-CC3).

## NOTES

The authors declare no competing financial interest.

## REFERENCES

Aguilera, D.A., Perez, A., Molina, R. and Moreno, S. (2011). Cu-Mn and Co-Mn catalysts synthesized from hydrotalcites and their use in the oxidation of VOCs. *Appl. Catal., B* 104: 144–150.

Chang, H., Wu, Q., Zhang, T., Li, M., Sun, X., Li, J., Duan, L. and Hao, J. (2015). Design strategies for $CeO_2$-$MoO_3$ catalysts for de$NO_x$ and $Hg^0$ oxidation in the presence of HCl: The significance of the surface acid-base properties. *Environ. Sci. Technol.* 49: 12388–12394.

Chen, W.K., Li, T.C., Sheu, G.R., Lin, N.H., Chen, L.Y. and Yuan, C.S. (2016). Correlation analysis, transportation mode of atmospheric mercury and criteria air pollutants, with meteorological parameters at two remote sites of mountain and offshore island in Asia. *Aerosol Air Qual. Res.* 16: 2692–2705.

Chi, G.L., Shen, B.X., Yu, R.R., He, C. and Zhang, X. (2017). Simultaneous removal of NO and $Hg^0$ over Ce-Cu modified $V_2O_5/TiO_2$ based commercial SCR catalysts. *J. Hazard. Mater.* 330*:* 83–92.

Chiu, C.H., Hsi, H.C. and Lin, C.C. (2014). Control of mercury emissions from coal-combustion flue gases using $CuCl_2$-modified zeolite and evaluating the cobenefit effects on $SO_2$ and NO removal. *Fuel Process. Technol.* 126: 138–144.

Chiu, C.H., Lin, H.P., Kuo, T.H., Chen, S.S., Su, K.H. and Hsi, H.C. (2015). Simultaneous control of elemental mercury/sulfur dioxide/nitrogen monoxide from coal fired flue gases with metal oxide-impregnated activated carbon. *Aerosol Air Qual. Res.* 15: 2094–2103.

Chou, C.P., Chang, T.C., Chiu, C.H. and Hsi, H.C. (2018) Mercury speciation and mass distribution in cement production process of Taiwan. *Aerosol Air Qual. Res.* 18: 2801–2812.

Di, W., Cheng, J.H., Tian, S.X., Li, J., Chen, J.Y. and Sun, Q. (2016). Synthesis and characterization of supported copper phyllosilicate catalysts for acetic ester hydrogenation to ethanol. *Appl. Catal., A* 510: 244–259.

Diaz, G., Perez-Hernandez, R., Gomez-Cortes, A., Benaissa, M., Mariscal, R. and Fierro, J.L.G. (1999). CuO-$SiO_2$ sol-gel catalysts: Characterization and catalytic properties for NO reduction. *J. Catal.* 187: 1–14.

Fang, D., Xie, J.L., Mei, D., Zhang, Y.M., He, F., Liu, X.Q. and Li, Y.M. (2014). Effect of $CuMn_2O_4$ spinel in Cu-Mn oxide catalysts on selective catalytic reduction of $NO_x$ with $NH_3$ at low temperature. *RSC Adv.* 4: 25540–25551.

Galbreath, K.C. and Zygarlicke, C.J. (2000). Mercury transformations in coal combustion flue gas. *Fuel Process. Technol.* 65: 289–310.

Gao, J., Yue, T., Zuo, P., Liu, Y., Tong, L., Wang, C., Zhang, X. and Qi, S. (2017). Current status and atmospheric mercury emissions associated with large-scale gold smelting industry in China. *Aerosol Air Qual. Res.* 17: 238–244.

He, J., Reddy, G.K., Thiel, S.W., Smirniotis, P.G. and Pinto, N.G. (2013). Simultaneous removal of elemental mercury and NO from flue gas using $CeO_2$ modified $MnO_x/TiO_2$ materials. *Energy Fuels* 27: 4832–4839.

He, S., Zhou, J.S., Zhu, Y.Q., Luo, Z.Y., Ni, M.J. and Cen, K.F. (2009). Mercury oxidation over a vanadia-based selective catalytic reduction catalyst. *Energy Fuels* 23: 253–259.

Jin, R.B., Liu, Y., Wang, Y., Cen, W.L., Wu, Z.B., Wang, H.Q. and Weng, X.L. (2014). The role of cerium in the improved $SO_2$ tolerance for NO reduction with $NH_3$ over Mn-Ce/$TiO_2$ catalyst at low temperature. *Appl. Catal., B* 148: 582–588.

Kang, M., Park, E.D., Kim, J.M. and Yie, J.E. (2006). Cu-Mn mixed oxides for low temperature NO reduction with $NH_3$. *Catal. Today* 111: 236–241.

Li, H.L., Li, Y., Wu, C.Y. and Zhang, J.Y. (2011a). Oxidation and capture of elemental mercury over $SiO_2$-$TiO_2$-$V_2O_5$ catalysts in simulated low-rank coal combustion flue gas. *Chem. Eng. J.* 169: 186–193.

Li, H.L., Wu, C.Y., Li, Y. and Zhang, J.Y. (2011b). $CeO_2$-$TiO_2$ catalysts for catalytic oxidation of elemental mercury in low-rank coal combustion flue gas. *Environ. Sci. Technol.* 45: 7394–7400.

Li, H.L., Wu, S.K., Li, L.Q., Wang, J., Ma, W.W. and Shih, K.M. (2015). CuO-$CeO_2$/$TiO_2$ catalyst for simultaneous NO reduction and $Hg^0$ oxidation at low temperatures. *Catal. Sci. Technol.* 5: 5129–5138.

Liu, K.H., Chen, M.Y., Tsai, Y.C., Lin, H.P. and Hsi, H.C. (2017). Control of $Hg^0$ and NO from coal-combustion flue gases using $MnO_x$-$CeO_x$/mesoporous $SiO_2$ from waste rice husk. *Catal. Today* 297: 104–112.

Marusczak, N., Castelle, S., de Vogüé, B., Knoery, J. and Cossa, D. (2016). Seasonal variations of total gaseous mercury at a French coastal Mediterranean site. *Aerosol Air Qual. Res.* 16: 46–60.

Presto, A.A. and Granite, E.J. (2006). Survey of catalysts for oxidation of mercury in flue gas. *Environ. Sci. Technol.* 40: 5601–5609.

Qiao, S.H., Chen, J., Li, J.F., Qu, Z., Liu, P., Yan, N.Q. and Jia, J.Q. (2009). Adsorption and catalytic oxidation of gaseous elemental mercury in flue gas over $MnO_x$/Alumina. *Ind. Eng. Chem. Res.* 48: 3317–3322.

Roy, S., Hegde, M.S. and Madras, G. (2009). Catalysis for $NO_x$ abatement. *Appl. Energy* 86: 2283–2297.

Shi, C., Chang, H., Wang, C., Zhang, T., Peng, Y., Li, M., Wang, Y. and Li, J. (2018). Improved activity and $H_2O$ resistance of Cu-modified $MnO_2$ catalysts for NO oxidation. *Ind. Eng. Chem. Res.* 57: 920–926.

Song, H., Zhang, M., Yu, J., Wu, W., Qu, R., Zheng, C. and Gao, X. (2018). The effect of Cr addition on $Hg^0$ oxidation and NO reduction over $V_2O_5$/$TiO_2$ catalyst. *Aerosol Air Qual. Res.* 18: 803–810.

Tang, C.J., Zhang, H.L. and Dong, L. (2016). Ceria-based catalysts for low-temperature selective catalytic reduction of NO with $NH_3$. *Catal. Sci. Technol.* 6: 1248–1264.

Tsai, C.Y., Chiu, C.H., Chuang, M.W. and Hsi, H.C. (2017). Influences of copper(II) chloride impregnation on activated carbon for low-concentration elemental mercury adsorption from simulated coal combustion flue gas. *Aerosol Air Qual. Res.* 17: 1637–1648.

UNEP (2013). Global Mercury Assessment 2013: Sources, Emissions, Releases and Environmental Transport. UNEP Chemicals Branch, Geneva, Switzerland https://wedocs.unep.org/handle/20.500.11822/7984, Last Access: September 2018.

U.S. EPA (2012). $SO_2$ and $NO_x$ emissions, compliance, and market analyses report. U.S. Environmental Protection Agency https://www.epa.gov/sites/production/files/2015-08/documents/arpcair12_01.pdf, Last Access: September 2018.

Wang, P.Y., Su, S., Xiang, J., Cao, F., Sun, L.S., Hu, S. and Lei, S.Y. (2013). Catalytic oxidation of $Hg^0$ by CuO-$MnO_2$-$Fe_2O$/γ-$Al_2O_3$ catalyst. *Chem. Eng. J.* 225: 68–75.

Wang, P.Y., Su, S., Xiang, J., You, H., Cao, F., Sun, L., Hu, S. and Zhang, Y. (2014). Catalytic oxidation of $Hg^0$ by $MnO_x$-$CeO_2$/γ-$Al_2O_3$ catalyst at low temperatures. *Chemosphere* 101: 19–54.

Wei, L., Cui, S.P., Guo, H.X., Ma, X.Y. and Zhang, L.J. (2016). DRIFT and DFT study of cerium addition on $SO_2$ of manganese-based catalysts for low temperature SCR. *J. Mol. Catal. A: Chem.* 421: 102–108.

Wu, Y.H., Xu, W.Q., Yang, Y., Wang, J. and Zhu, T.Y. (2018). Support effect of Mn-based catalysts for gaseous elemental mercury oxidation and adsorption. *Catal. Sci. Technol.* 8: 297–306.

Xiong, S.C., Xiao, X., Huang, N., Dang, H., Liao, Y., Zou, S.J. and Yang, S.J. (2017). Elemental mercury oxidation over Fe-Ti-Mn spinel: Performance, mechanism, and reaction kinetics. *Environ. Sci. Technol.* 51: 531–539.

Xu, L., Wang, C., Chang, H., Wu, Q., Zhang, T. and Li, J. (2018). New insight into $SO_2$ poisoning and regeneration of $CeO_2$-$WO_3$/$TiO_2$ and $V_2O_5$-$WO_3$/$TiO_2$ catalyst for low-temperature $NH_3$-SCR. *Environ. Sci. Technol.* 52: 7064–7071.

Yan, Q.H., Chen, S.N., Qiu, L., Gao, Y.S., O'Hare, D. and Wang, Q. (2018). The synthesis of $Cu_yMn_zAl_{1-z}O_x$ mixed oxide as a low-temperature $NH_3$-SCR catalyst with enhanced catalytic performance. *J. Chem. Soc., Dalton Trans.* 47: 2992–3004.

Yang, S.J., Guo, Y.F., Chang, H.Z., Ma, L., Peng, Y., Qu, Z., Yan, N.Q., Wang, C.Z. and Li, J.H. (2013). Novel effect of $SO_2$ on the SCR reaction over $CeO_2$: Mechanism and significance. *Appl. Catal., B* 136–137: 19–28.

Yi, Y.Y., Li, C.T., Zhao, L.K., Du, X.Y., Gao, L., Chen, J.Q., Zhai, Y.B. and Zeng, G.M. (2018). The synthetic evaluation of CuO-$MnO_x$-modified pinecone biochar for simultaneous removal formaldehyde and elemental mercury from simulated flue gas. *Environ. Sci. Pollut. Res.* 25: 4761–4775.

Yu, X.N., Cao, F.F., Zhu, X.B., Zhu, X.C., Gao, X., Luo, Z.Y. and Cen, K.F. (2017). Selective catalytic reduction of NO over Cu-Mn/OMC catalysts: Effect of preparation method. *Aerosol Air Qual. Res.* 17: 302–313.

Yue, H., Zhao, Y., Zhao, S., Wang, B., Ma, X. and Gong, J. (2013). A copper-phyllosilicate core-sheath nanoreactor for carbon-oxygen hydrogenolysis reactions. *Nat. Commun.* 4: 2339.

Zhang, D.S., Zhang, L., Shi, L.Y., Fang, C., Li, H.R., Gao, R.H., Huang, L. and Zhang, J.P. (2013). In situ supported $MnO_x$-$CeO_x$ on carbon nanotubes for the low-temperature selective catalytic reduction of NO with $NH_3$. *Nanoscale* 5: 1127–1136.

Zhao, H., Mu, X., Zheng, C., Liu, S., Zhu, Y., Gao, X. and Wu, T. (2019). Structural defects in 2D $MoS_2$ nanosheets and their roles in the adsorption of airborne elemental mercury. *J. Hazard. Mater.* 366: 240–249.

Zhao, L.K., Li, C.T., Li, S.H., Wang, Y., Zhang, J.Y., Wang, T. and Zeng, G.M. (2016). Simultaneous removal of elemental mercury and NO in simulated flue gas over $V_2O_5$/$ZrO_2$-$CeO_2$ catalyst. *Appl. Catal., B* 198: 420–430.

*Received for review, October 31, 2018*
*Revised, April 1, 2019*
*Accepted, May 1, 2019*